Wannier functions using a discrete variable representation for optical lattices

Saurabh Paul*
Joint Center for Quantum Information and Computer Science, Joint Quantum Institute and University of Maryland, Maryland 20742, USA

Eite Tiesinga
Joint Quantum Institute and Joint Center for Quantum Information and Computer Science, National Institute of Standards and Technology and University of Maryland, Gaithersburg, Maryland 20899, USA

(Received 30 March 2016; published 7 September 2016)

We propose a numerical method using the discrete variable representation (DVR) for constructing real-valued Wannier functions localized in a unit cell for both symmetric and asymmetric periodic potentials. We apply these results to finding Wannier functions for ultracold atoms trapped in laser-generated optical lattices. Following S. Kivelson [Phys. Rev. B **26**, 4269 (1982)], for a symmetric lattice with inversion symmetry, we construct Wannier functions as eigenstates of the position operators $\hat{x}$, $\hat{y}$, and $\hat{z}$ restricted to single-particle Bloch functions belonging to one or more bands. To ensure that the Wannier functions are real-valued, we numerically obtain the band structure and real-valued eigenstates using a uniform Fourier grid DVR. We then show, by a comparison of tunneling energies, that the Wannier functions are accurate for both inversion-symmetric and asymmetric potentials to better than 10 significant digits when using double-precision arithmetic. The calculations are performed for an optical lattice with double-wells per unit cell with tunable asymmetry along the x axis and a single sinusoidal potential along the perpendicular directions. Localized functions at the two potential minima within each unit cell are similarly constructed, but using a superposition of single-particle solutions from the two lowest bands. We finally use these localized basis functions to determine the two-body interaction energies in the Bose-Hubbard model and show the dependence of these energies on lattice asymmetry.

DOI: 10.1103/PhysRevA.94.033606

I. INTRODUCTION

Ultracold atoms in optical lattices form highly tunable systems and are increasingly used to simulate complex quantum many-body Hamiltonians [1,2]. The now very commonly used Bose-Hubbard (BH) model was first proposed in the context of cold atoms in Ref. [3], and its interaction-driven quantum phase transition in a cubic lattice was subsequently observed in [4]. Since then, more exotic lattice geometries such as double-well lattices [5–8], honeycomb, triangular, and Kagome lattices [9,10], and artificial graphene [11,12] have been experimentally realized. This has vastly expanded the standard BH model to include additional terms ranging from excited band contributions, to beyond-nearest-neighbor tunneling, to richer on-site and off-site atom-atom interactions [13–16]. In conjunction, there has been a growing need to quantitatively model these systems with greater accuracy.

BH models are an approximation to the full many-body Hamiltonian in the tight-binding (TB) limit and are written in a single-particle basis of spatially localized wave functions, generally referred to as Wannier functions. The parameters of the BH model are obtained as integrals over these functions. Thus, the key to accurately model these systems is to first construct a set of properly localized orthonormal basis functions. For simple cubic lattices with inversion symmetry, the standard procedure is to construct Wannier functions as "simple" superpositions of the Bloch functions belonging to a *single* energy band [17,18]. For more complex lattice geometries with either asymmetries or quasidegenerate energy bands, this procedure, however, does not lead to basis functions localized at the potential minima within each unit cell.

A common approach to ensuring localized Wannier functions for atoms in optical lattices is to use nonorthogonal atomic orbitals, modeled as harmonic oscillator wave functions near the potential minima [11,19]. This underestimates the tunneling energies even for deep lattices where the harmonic approximation is expected to work better. A more general approach developed within the solid-state community is due to Marzari and Vanderbilt [20,21], where maximally localized Wannier functions are constructed by minimizing its spread by a suitable gauge transformation of the composite Bloch functions. This scheme has been adapted for atoms in optical lattices [22–26]. Wannier functions obtained using this method, however, are not guaranteed to be real-valued and in turn depend on the choice of gauge transformation. An alternate method for constructing Wannier functions is by minimization of density-induced tunneling and density-density interactions between neighboring unit cells [27].

In this paper, we propose an alternative numerical scheme for constructing real-valued Wannier functions. Following Kivelson [28], who showed that for an inversion-symmetric lattice, Wannier functions are eigenstates of the position operator, we construct Wannier functions by diagonalization of the position operator expressed in the eigenstates of the single-particle Hamiltonian. The localized functions are remarkably accurate even for lattices with a large asymmetry. To ensure that the Wannier functions are strictly real-valued, we obtain the band structure and corresponding real-valued eigenfunctions using a uniform Fourier-grid discrete variable representation (DVR) [29]. General background on the DVR method can be found in [30–33], and some of their uses

*pauls@umd.edu

in ultracold atomic systems can be found in [34] and [35]. Generalized Wannier functions localized at the potential minima in a unit cell are similarly constructed using a superposition of Bloch functions of multiple bands.

The proposed method does not suffer from the problems of local minima, as is sometimes the case with the Marzari and Vanderbilt approach of constructing Wannier functions [25]. In addition, using the DVR approach intrinsically ensures that the Wannier functions are real-valued. This differs from the alternative method, which uses time-reversal symmetry to construct real-valued single-particle basis functions using a superposition of Bloch functions of opposite quasimomenta [12].

The remainder of the paper is set up as follows. In Sec. II, we introduce the asymmetric double-well optical lattice potential, for which we describe the numerical procedure to obtain real-valued DVR-based Wannier functions. The method can be used for general lattices. For clarity, we focus on a particular lattice potential. In Sec. III, we discuss how the single-particle band structure for this lattice can be obtained using a DVR and, also, how it compares with that of a plane-wave (PW) basis calculation. We also describe how to extend our approach to general lattices. In Sec. IV real-valued Wannier and localized functions within a double-well potential are obtained using the eigenvectors from the DVR calculations. In Sec. V, we discuss the accuracy of these numerically obtained Wannier functions by comparing the tunneling energies obtained using these functions to those obtained using a Fourier transform of the band dispersion. We use these DVR-based Wannier functions in Sec. VI to compute the two-body interaction energies for various asymmetries. We conclude in Sec. VII.

II. OPTICAL LATTICE POTENTIAL

We consider optical lattice potentials that have a double-well structure along the x axis and a single-well structure along the perpendicular y and z axes. Such a lattice can be constructed using a laser with wave vector k_L and its first harmonic. The potential is given by

$$V(\vec{x}) = -V_0\cos^2(k_L x) - V_1\cos^2[2k_L(x+b)] - V_2[\cos^2(2k_L y) + \cos^2(2k_L z)], \quad (1)$$

where $V_{0,1,2} > 0$ are lattice depths. The lattice has periodicity $a = \pi/k_L$ along the x axis and $a/2$ along the perpendicular directions. The displacement b determines whether the lattice has an inversion-symmetric or asymmetric double-well. It is inversion symmetric for $k_L b = \pi/4$ and asymmetric otherwise. Throughout, we express energies in units of the recoil energy $E_R = \hbar^2 k_L^2/(2m_a)$, where m_a is the atomic mass. Figure 1(a) shows a contour plot of the optical lattice potential in the xy plane for $k_L b = 0.21\pi$, while Fig. 1(b) shows the corresponding asymmetric double-well along the x axis. We concentrate on the potential along the x axis in subsequent sections. The perpendicular directions are needed when estimating two-body interaction energies in Sec. VI.

III. BAND STRUCTURE USING A DISCRETE VARIABLE REPRESENTATION

The single-particle band structure of a periodic potential is generally numerically determined in a plane-wave basis. For

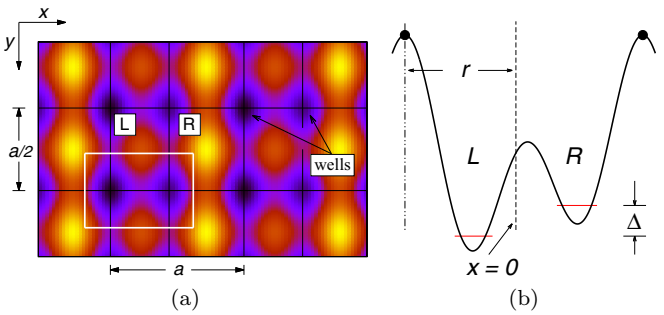

FIG. 1. (a) Contour plot of the optical lattice potential in the xy plane, where the potential minima are in dark blue. The white box encloses a unit cell of length a and $a/2$ along x and y, respectively. Each unit cell has a double-well along the x axis, labeled L and R, and a single well along the y and z axes. (b) An asymmetric double-well potential (black curve) as a function of x for $V_1/V_0 = 1.3$ and $k_L b = 0.21\pi$. Horizontal red curves in the L and R wells represent the lowest two single-particle energy levels. The energy gap between these levels is Δ. The separation between the black dots is the lattice period a. The origin $x = 0$ of our coordinate system is indicated by the dashed line. For a symmetric lattice, the origin lies at the top of the barrier between the L and the R wells. The distance between the origin and the left black dot is r.

asymmetric lattices, the eigenvectors or the Bloch functions in this basis are complex-valued and the corresponding Wannier functions are complex as well. We use a discrete variable representation to obtain real-valued eigenfunctions.

We begin the procedure by discussing the one-dimensional DVR along the x axis. We are interested in solutions that have periodic boundary conditions over M_x unit cells. For our double-well potential, it is convenient to apply the shift $x \to x - r$ such that the origin of the x axis coincides with the top of the potential barrier (see Fig. 1) and consider the interval $(0, M_x a)$. For a symmetric double-well $r = a/2$, while, in general, it depends on the symmetry parameter b. We now introduce the uniformly spaced Fourier grid [29], based on $2N_x + 1$ periodic orthonormal basis functions $\phi_n(x) = \exp[i2\pi nx/(M_x a)]/\sqrt{M_x a}$ for $n = 0, \pm 1, \ldots, \pm N_x$. Orthonormal DVR basis functions are $f_i(x) = \langle x|x_i\rangle = \sqrt{\Delta x}\sum_{n=-N_x}^{N_x}\phi_n^*(x_i)\phi_n(x)$, labeled by grid points $x_i = i\Delta x$ with $i = 1, \ldots, 2N_x + 1$ and $\Delta x = M_x a/(2N_x + 1)$. A function $\langle x|x_i\rangle$ is localized around x_i and can be simplified with some trigonometry.

In this representation of grid points, the kinetic energy operator is $T_{ii'} = \langle x_i|T|x_{i'}\rangle$, where

$$T_{ii'} = (-1)^{i'-i}E_R\left(\frac{2\pi}{M_x k_L a}\right)^2 \times \begin{cases} N_x(N_x+1)/3, & i = i', \\ \dfrac{\cos[\pi(i'-i)/(2N_x+1)]}{2\sin^2[\pi(i'-i)/(2N_x+1)]}, & i \neq i', \end{cases} \quad (2)$$

and to a good approximation the potential energy operator is $\langle x_i|V|x_{i'}\rangle = V(x_i)\delta_{ii'}$ with Kronecker delta δ_{ij}. In fact, it is this approximation that will limit our numerical accuracy using the DVR. On the other hand, the single-particle Hamiltonian $H_0 = T + V$ is a real symmetric matrix for both symmetric and asymmetric lattice potentials and its eigenfunctions can

always be obtained using real arithmetic. We note that in a PW basis, the Hamiltonian for an asymmetric lattice is a complex Hermitian matrix. Typically, we require that $2N_x + 1 \gg M_x$, leading to many grid points per unit cell.

The eigenfunctions $|\lambda\rangle$ with dispersion energy ϵ_λ of H_0 with $\lambda \in \{1, \ldots, 2N_x + 1\}$ can be grouped into N_{band} bands containing M_x discrete quasimomenta. This implies that both N_{band} and M_x must be odd, as $M_x N_{\text{band}} = 2N_x + 1$. In fact, the lowest M_x eigenenergies correspond to the first band, the next set corresponds to the second band, and so on. It can be separately shown from the $\phi_n(x)$ that the allowed quasimomenta are

$$k_x = \frac{2p}{M_x}\frac{\pi}{a}, \quad p = 0, \pm 1, \pm 2, \ldots, \pm\frac{1}{2}(M_x - 1), \qquad (3)$$

such that $-\pi/a \leqslant k_x \leqslant \pi/a$ and k_x stays within the first Brillouin zone. It is noteworthy that N_{band} also corresponds to the number of grid points within each unit cell. For real potentials $V(x)$, the eigenenergies for $\pm k_x$ are degenerate. Consequently, the single eigenstate with zero quasimomentum can be easily located from the dispersion ϵ_λ. For other quasimomenta, we can locate the pair of real eigenfunctions with degenerate ϵ_λ and compute the 2×2 matrix of the momentum operator. The eigenvalues of the momentum operator give the quasimomentum k_x, thus leading to the assignment of the band dispersion $\epsilon_\lambda \to \epsilon_\alpha(k_x)$ with band index α. (Diagonal elements of the momentum operator are strictly 0, as the eigenfunctions of H_0 are real and periodic in interval $[0, M_x a]$).

Figure 2(a) shows numerical results for the double-well band dispersion at $k_x = 0$ for the lowest two bands using the PW basis. We find that energy differences become "noisy" beyond $N_{\text{PW}} > 25$ basis vectors and convergence is reached with uncertainties of $2\times10^{-12} E_R$ independent of the lattice asymmetry and band. This uncertainty should be compared with the band gap, $\approx\Delta$, between the two bands, which is of the order of E_R for typical lattice depths and is close to the numerical accuracy to be expected using double-precision arithmetic. Figure 2(b) shows similar data, but obtained for the DVR calculations as a function of N_{band} and $M_x = 3$. The integers N_{band} and N_{PW} can be directly compared, as they both correspond to the number of energy bands obtained within the corresponding calculation. We find that convergence is reached for $N_{\text{band}} > 25$ with uncertainties of $2\times10^{-11} E_R$ independent of the lattice asymmetry and band. For PW calculations with $N_{\text{PW}} > 25$ and DVR calculations with $N_{\text{band}} > 25$, the largest uncertainty is independent of the quasimomentum.

Figure 2(c) compares the $k_x = 0$ band dispersion computed with the DVR and PW basis, respectively. It shows that for symmetric lattices, the DVR and PW results agree to within the uncertainty of the DVR calculation. For asymmetric lattices, however, they converge to different values. The inset further highlights the difference between symmetric and asymmetric lattices by studying the difference of the band dispersion as a function of the lattice asymmetry $k_L b$. We find that the value of $\epsilon_\alpha(k_x = 0)$ for the DVR is always larger than the PW result and the difference is symmetric around $k_L b = \pi/4$. The two results only agree infinitesimally close to $k_L b = \pi/4$. Furthermore, we find that the discrepancy is the same independent of the quasimomentum. As we show in Sec. V, this constant offset, nevertheless, leads to tunneling energies that are more accurate than might naively be expected.

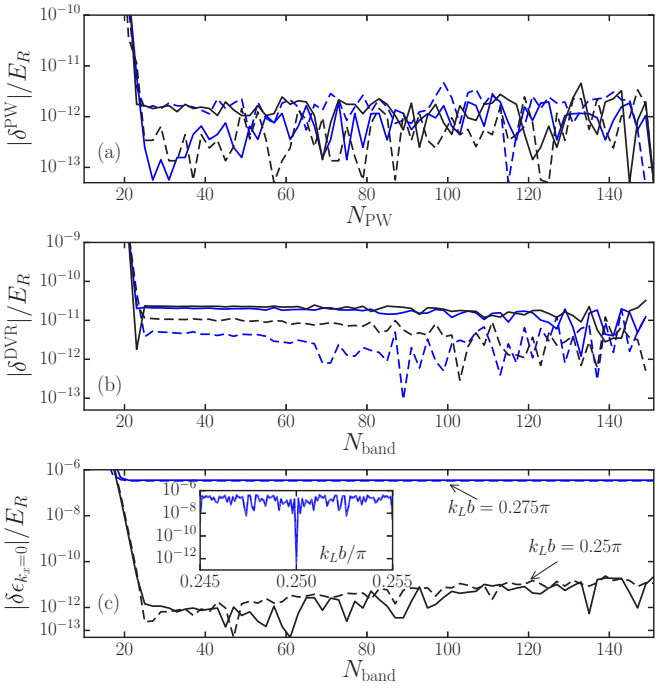

FIG. 2. (a) Convergence of the energy dispersion $\epsilon_\alpha(k_x)$ at quasimomentum $k_x = 0$ computed with a plane-wave (PW) basis as a function of N_{PW}, the number of PWs. We plot the difference $\delta^{\text{PW}}(N_{\text{PW}}) = \epsilon_\alpha(k_x = 0; N_{\text{PW}}) - \epsilon_\alpha(k_x = 0; N_{\text{PW}}^{\text{max}})$, where $N_{\text{PW}}^{\text{max}} = 151$. (b) A similar convergence plot using a discrete variable representation (DVR) basis as a function of N_{band}, the number of grid points in a unit cell. Plotted is $\delta^{\text{DVR}}(N_{\text{band}}) = \epsilon_\alpha(k_x = 0; N_{\text{band}}) - \epsilon_\alpha(k_x = 0; N_{\text{band}}^{\text{max}})$, where $N_{\text{band}}^{\text{max}} = 151$ and $M_x = 3$. (c) Comparison of $\epsilon_\alpha(k_x)$ at $k_x = 0$ obtained using the DVR and PW basis. We plot $\delta(N_{\text{band}}) = \epsilon_\alpha(k_x = 0; \text{DVR}) - \epsilon_\alpha(k_x = 0; \text{PW})$ as a function of N_{band}. PW results are obtained with 151 basis vectors. In all panels black and blue curves are for a symmetric lattice with $k_L b = \pi/4$ and an asymmetric lattice with $k_L b = 0.275\pi$, respectively. Solid and dashed lines correspond to bands $\alpha = 1$ and 2, respectively, and lattice depths are $V_0 = 35 E_R$ and $V_1/V_0 = 1.3$, where E_R is the recoil energy. Inset in (c) DVR and PW results as a function of the lattice asymmetry $k_L b$ for fixed $N_{\text{band}} = N_{\text{PW}} = 51$.

Although we have focused on DVR-based band structure calculations for a one-dimensional lattice, the method can be extended to higher-dimensional nonseparable lattices, such as graphene. The simplest approach is based on the realization that it is always possible to construct a nonprimitive unit cell with orthogonal unit vectors such that the higher-dimensional kinetic-energy operator is separable along the unit vector directions and Eq. (2) can be directly used. Alternatively, we construct DVR basis functions from PWs that are periodic over a multiple of the primitive lattice vectors. In this case, the kinetic energy is not separable but can still be expressed in terms of trigonometric functions. We note, however, that for a d-dimensional lattice the matrix size of the single-particle Hamiltonian in the DVR method will be M^d times the size of the corresponding PW matrix, where M is the number of discrete quasimomentum points along an axis. This implies

that the determination of the eigenpairs with the DVR method is computationally more intensive but is guaranteed to lead to real-valued eigenvectors.

IV. DVR-BASED WANNIER FUNCTIONS

In this section we numerically construct real-valued Wannier functions localized within unit cells and generalized Wannier functions localized near the potential minina in each double-well from superpositions of our real-valued DVR eigenfunctions. Here, we describe a method for constructing these Wannier functions based on Refs. [28] and [12].

Kivelson [28] showed that for symmetric lattices with inversion symmetry, real-valued Wannier functions for band α are eigenstates of the projected position operator $\hat{x}_\alpha = \mathcal{P}_\alpha\, \hat{x}\, \mathcal{P}_\alpha$, where $\mathcal{P}_\alpha$ is the projection operator on the eigenstates of band α. The spacing between neighboring eigenvalues of this projected operator is a lattice constant.

We extend this approach for constructing real-valued Wannier functions to both symmetric and asymmetric lattices lacking inversion symmetry, even though there is no formal proof that for asymmetric lattices eigenfunctions of the position operator are Wannier functions. We term our functions "DVR-based" Wannier functions. Following the previous section, the DVR eigenfunctions $|\lambda\rangle$ can be grouped into bands α. In fact, we have $|\lambda\rangle = |m,\alpha\rangle$, with $m \in \{1,\ldots,M_x\}$ and projector $\mathcal{P}_\alpha = \sum_m |m,\alpha\rangle\langle m,\alpha|$. We construct the matrix $\langle m,\alpha|\hat{x}|m',\alpha\rangle$ over all m and m' in the same band α using that $\langle x_i|\hat{x}|x_{i'}\rangle = x_i\delta_{ii'}$ to good approximation. Diagonalization leads to real DVR-based Wannier functions $w_{j,\alpha}(x)$ for unit cell $j = \{1,\ldots,M_x\}$, and as we show in Sec. V, they reproduce the tunneling energies with great accuracy.

Generalized Wannier functions $v_{j,\eta}(x)$ localized in the $\eta = L$ and R wells in Fig. 1 can be constructed by creating superpositions of DVR functions from multiple bands. In our case, we restrict the bands to $\alpha \in \{1,2\}$ and compute the eigenfunctions of the projected position operator $\mathcal{P}\hat{x}\mathcal{P}$, where $\mathcal{P} = \sum_{m,\alpha=1,2} |m,\alpha\rangle\langle m,\alpha|$. This approach is used for both symmetric and asymmetric lattices.

Figures 3(a) and 3(d) show numerical Wannier functions $w_{j,\alpha}(x)$ for a symmetric lattice with band index $\alpha \in \{1,2\}$ on a linear and logarithmic scale, respectively. The Wannier function is localized in the unit cell at the center of the lattice with $j = j_c \equiv (M_x+1)\text{div}2$ and $x_c = M_x a/2$. For the symmetric lattice, both $w_{j_c,1}(x)$ and $w_{j_c,2}(x)$ are, however, spread over the two wells in the unit cell. Figures 3(b) and 3(e) show similar plots for an asymmetric lattice, while Figs. 3(c) and 3(f) show generalized Wannier functions $v_{j_c,\eta}(x)$ with $\eta \in \{L,R\}$ based on the first two bands for the same lattice parameters. Owing to the large asymmetry for the latter four panels, the band gap between the two lowest bands is large. We thus expect $w_{j_c,1}(x) \approx w_{j_c,R}(x)$ and $w_{j_c,2}(x) \approx w_{j_c,L}(x)$, as is indeed observed when comparing Figs. 3(b) and 3(c). It is, however, interesting to note that the $v_{j_c,\eta}(x)$'s and $w_{j_c,\alpha}(x)$'s are not exactly the same. In fact, $v_{j_c,\eta}(x)$ is more localized within the L and R wells compared to $w_{j_c,\alpha}(x)$. For even larger asymmetries, this difference in localization persists and the "tail" of $w_{j_c,\alpha}(x)$ does not approach $v_{j_c,\eta}(x)$, leading to marked differences in the calculated BH parameters, as shown in Sec. VI.

Figure 4 shows a comparison of Wannier functions for a symmetric lattice computed at different unit cells. We find that the difference between the Wannier functions at the edge and the center is of the order of $10^{-5}/\sqrt{M_x a}$ for all x. For all other unit cells, the difference from the central Wannier

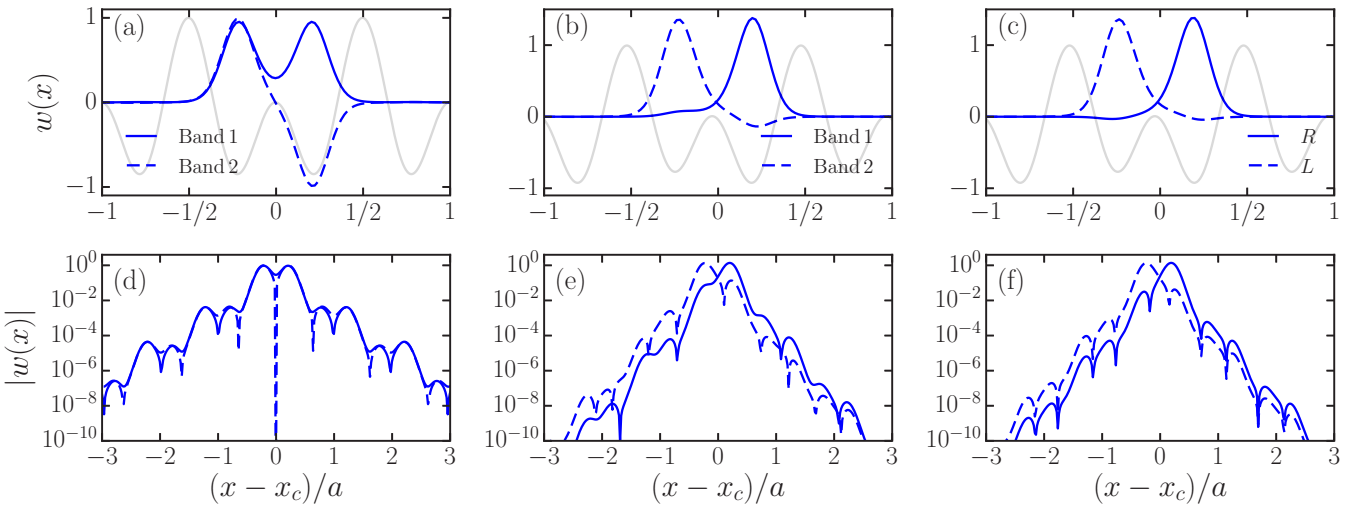

FIG. 3. Plots of normalized Wannier functions $w_{j_c,\alpha}(x)$ and generalized Wannier functions $v_{j_c,\eta}(x)$ in the center of the lattice as a function of x. Here, wave functions and position are in units of $1/\sqrt{M_x a}$ and lattice period a, respectively. (a, d) The $\alpha = 1,2$ Wannier functions for a symmetric lattice on a linear (a) and a logarithmic (d) scale. For clarity, we have shifted the x axis by x_c, such that the center of the interval is at the origin. Here, $M_x = 21$, $N_{\text{band}} = 53$, $k_L b = 0.25\pi$, $V_0/E_R = 35$, and $V_1/V_0 = 1.3$. Solid and dashed blue curves represent the first and second bands, respectively. The gray line represents the symmetric double-well potential. (b), (e) Similar plots, but for an asymmetric lattice with $k_L b = 0.275\pi$ and other parameters unchanged. (c), (f) Generalized Wannier functions at the L and R wells within a double-well for the same lattice as used in (b) and (e). Solid and dashed blue lines represent $v_{j_c,R}(x)$ and $v_{j_c,L}(x)$, respectively.

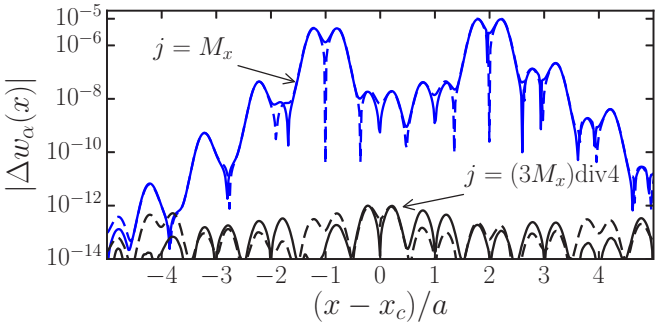

FIG. 4. Graphs of the difference between the (shifted) Wannier functions $w_{j,\alpha}(x)$ and that at the center of the lattice. Plotted are $\Delta w_\alpha(x) = |w_{j,\alpha}(x - [j - j_c]a)| - |w_{j_c,\alpha}(x)|$ for unit cells $j = (3M_x)\text{div}4$ (black curves) and M_x (blue curves) as a function of x in units of lattice period a. The argument $x - [j - j_c]a$ is computed assuming modular arithmetic in interval $M_x a$. Solid and dashed lines correspond to bands $\alpha = 1$ and 2, respectively. The plot is for a symmetric lattice with $k_L b = 0.25\pi$, $V_0 = 35E_R$, $V_1/V_0 = 1.3$, $M_x = 21$, and $N_{\text{band}} = 53$.

function is of the order of $10^{-13}/\sqrt{M_x a}$, which is close to our numerical accuracy. One such difference with $j = (3M_x)\text{div}4$ is shown in the figure. Hence, the shapes of our DVR-based Wannier functions are mostly independent of the unit cell. This observation remains true for asymmetric lattices.

V. TUNNELING ENERGIES BASED ON DVR-BASED WANNIER FUNCTIONS

In Sec. IV we showed that the Wannier functions and generalized Wannier functions within a double-well can be constructed from DVR eigenvectors. In this section we use these functions to compute tunneling energies and discuss their accuracy. In particular, the accuracy of the single-band Wannier functions are ascertained in Sec. V A by comparing band tunneling energies, as they depend only on the band dispersion and should be independent of the choice of Wannier functions. Tunneling energies between neighboring L and R wells are computed in Sec. V B and a corresponding tight-binding model is shown to have significant contributions from tunneling energy terms between next-nearest neighbors and beyond.

A. Band tunneling energies

Tunneling energies are defined by the matrix elements $J_\alpha = \langle w_{j,\alpha}|H_0|w_{j',\alpha}\rangle$ over the Wannier functions of band α localized in unit cells j and j'. Here, H_0 is the single-particle Hamiltonian. We mainly focus on nearest-neighbor tunneling with $j' = j \pm 1$. Formally, the J_α should depend only on $|j - j'|$.

There are three ways to obtain tunneling energies. The first is to use our DVR-based Wannier functions for band α as computed in Sec. IV and calculate the matrix element. We label them J_α^{W}. The other two methods rely on the usual definition of a Wannier function as a "Fourier transform" of Bloch functions of the corresponding band. With this definition, the tunneling energies depend only on the band dispersion $\epsilon_\alpha(k_x)$ and between nearest-neighbor unit cells ($|j - j'| = 1$) is given by

$$J_\alpha = \frac{a}{2\pi}\int_{-\pi/a}^{\pi/a} \cos(k_x a)\epsilon_\alpha(k_x)dk_x, \tag{4}$$

independent of j. The tunneling energy can now be determined either by substituting $\epsilon_\alpha(k_x)$ calculated using the PW basis or by using the band dispersion obtained from the DVR method. We refer to these tunneling energies as J_α^{PW} and J_α^{DVR}, respectively.

Figure 5 shows a comparison between tunneling energies J_α^{PW}, J_α^{DVR}, and J_α^{W} as a function of the number of unit cells. The energy J_α^{W} has been computed using "DVR-based" Wannier function for the central unit cell. We find that for a symmetric lattice Fig. 5(a)] convergence is reached for $M_x > 9$ unit cells, with uncertainties of $2\times10^{-13}E_R$ for all methods. This confirms the central idea of Ref. [28], that Wannier functions are eigenstates of the $\hat{x}_\alpha$ operator for symmetric lattices. Figure 5(b) shows that $J_\alpha^{\text{DVR}} - J_\alpha^{\text{PW}}$ and $J_\alpha^{\text{W}} - J_\alpha^{\text{PW}}$ converge to $2\times10^{-11}E_R$ for band 1 and $1\times10^{-10}E_R$ for band 2, far above the value reached for the symmetric lattice. Within the DVR calculation, however, J_α^{W} and J_α^{DVR} agree much better. The discrepancy between the PW and the DVR results can be attributed to the difference in the band dispersion shown in Fig. 2. Nevertheless, even an uncertainty of $10^{-10}E_R$ is sufficient for all practical purposes.

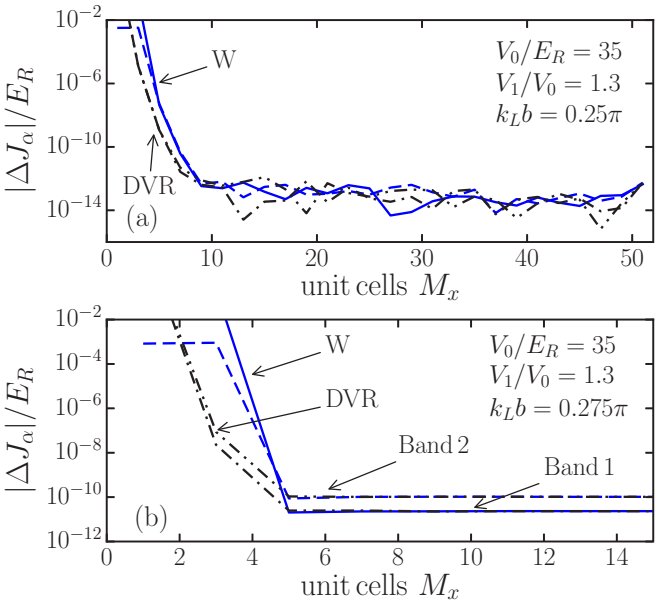

FIG. 5. Comparison of the nearest-neighbor tunneling energies J_α^{PW}, J_α^{DVR}, and J_α^{W} for bands $\alpha = \{1,2\}$, as computed using the Fourier transform of the band dispersion from the PW and DVR calculations and the DVR band Wannier functions $w_\alpha(x)$, respectively. (a) Tunneling energy comparison for a symmetric lattice with $k_L b = 0.25\pi$. Plotted are $\Delta J_\alpha = J_\alpha^{\text{DVR}} - J_\alpha^{\text{PW}}$ (black curves labeled "DVR") and $\Delta J_\alpha = J_\alpha^{\text{W}} - J_\alpha^{\text{PW}}$ (blue curves labeled "W") in units of E_R as a function of the number of unit cells M_x. Solid and dashed lines correspond to bands $\alpha = 1$ and 2, respectively. We used $V_0 = 35E_R$, $V_1/V_0 = 1.3$, and $N_{\text{PW}} = N_{\text{band}} = 35$. (b) Similar plot for an asymmetric lattice with $k_L b = 0.275\pi$ and other parameters unchanged.

We have numerically ascertained that J_α^{W} does not vary with the unit cell index j to better than $10^{-13}E_R$ apart from the two edge unit cells, consistent with our observations on the shape of Wannier functions in Fig. 4. In fact, the difference in the tunneling energies at the central versus the edge unit cell is only $10^{-8}E_R$. Consequently, the value of J_α^{W} obtained from the central unit cell is better than that from the edge unit cells and agrees better with J_α^{PW}. In other words, a comparison with the tunneling energies J_α^{PW} gives a good estimate of the accuracy of our real-valued Wannier functions.

We have also determined the next-nearest-neighbor tunneling energies. For typical lattice depths, its value is two orders of magnitude or more lower than that of nearest neighbors. Its uncertainty in units of E_R is the same as for nearest-neighbor tunneling energies. Hence, we conclude that the DVR-based Wannier functions can be used to compute tunneling energies between distant neighbors.

B. Tight-binding tunneling energies

It is often useful to write down a TB Hamiltonian in terms of L and R wells defined in Fig. 1 with hopping parameters computed from our generalized Wannier functions with the lowest on-site energies $\langle v_{j,\eta}|H_0|v_{j',\eta}\rangle$. Figure 6 defines tunneling energies between adjacent unit cells and the energy gap Δ between the on-site energies based on the lowest two bands of our H_0. The largest parameters are given by $t = \langle w_{j,L}|H_0|w_{j,R}\rangle$ and $J = \langle w_{j,R}|H_0|w_{j+1,L}\rangle$, where j is the unit cell index. Similar expressions can be written for other parameters. The value of these tunneling energies depends on the definition of the generalized Wannier functions and cannot be extracted from a transformation of the band dispersion energies. Finally, we note that all coefficients are real-valued.

Figure 7 shows the seven largest hopping parameters of our TB model as a function of the lattice depth V_0 for an asymmetric lattice. As expected, the tunneling energies decrease with the lattice depth, while simultaneously Δ increases. For a fixed lattice depth the tunneling energies are lower the farther the atom has to hop.

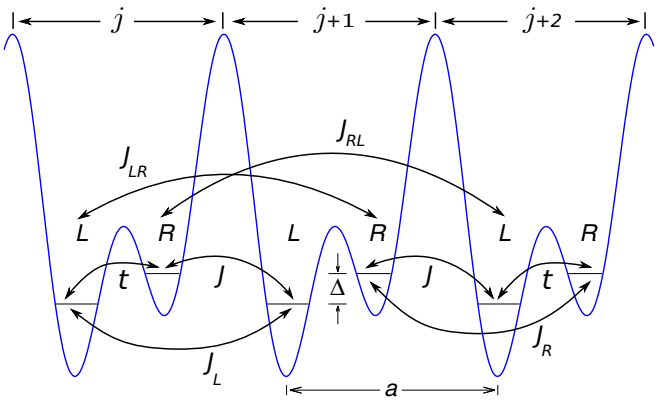

FIG. 6. Tight-binding Hamiltonian based on the lowest two bands for an asymmetric double-well optical lattice. Various tunneling energies t, J, J_L, J_R, J_{LR}, and J_{RL} between three neighboring unit cells are shown. The energy gap between the two on-site energies is Δ and the lattice has period a.

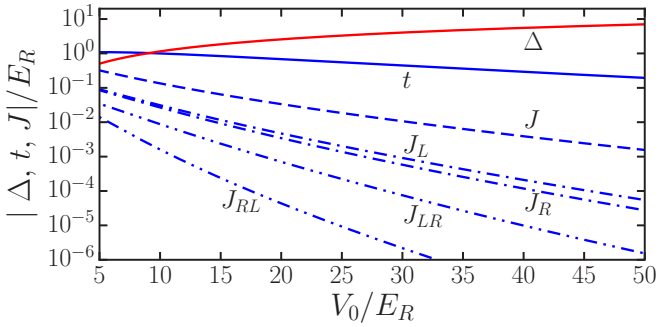

FIG. 7. Log-linear plot of the absolute value of tunneling energies t, J, J_L, J_R, J_{LR}, and J_{RL} and energy gap Δ in units of E_R as a function of the lattice depth V_0. The plot is for an asymmetric lattice with $k_L b = 0.275\pi$ and $V_1/V_0 = 1.3$.

The TB Hamiltonian for two modes within a unit cell can be diagonalized analytically by a transformation to quasimomentum space. In fact, the eigenenergies are

$$\epsilon_\alpha^{\mathrm{TB}}(k_x) = -(J_R + J_L)\cos k_x a \mp \sqrt{[(J_R - J_L)\cos k_x a - \Delta/2]^2 + |f(k_x)|^2}, \quad (5)$$

where $\mp$ corresponds to bands $\alpha = 1$ and 2, respectively, and $f(k_x) = t + Je^{-ik_x a} + J_{LR}e^{ik_x a} + J_{RL}e^{-2ik_x a}$. The band tunneling energies J_α^{TB} can be obtained by substituting $\epsilon_\alpha^{\mathrm{TB}}(k_x)$ into Eq. (4) and performing the Fourier transform.

We can now compare the band tunneling energies of our TB simulations with those of the exact band structure calculations using the PW basis. We find that the difference between the TB and PW result is within approximately 50% for both bands when we only include nearest-neighbor tunneling energies t and J and 5% when, in addition, next-nearest-neighbor tunneling energies J_L and J_R are included, and this stays nearly the same upon including the next-to-next-nearest-neighbor hopping terms J_{LR} and J_{RL}. These differences are almost independent of the lattice depth and consistent with results in Ref. [23], where the calculations were based on complex-valued maximally localized Wannier functions. The TB result can be improved if we include more tunneling energies and allow atoms to hop even further.

VI. INTERACTION ENERGIES

We have shown the excellent accuracy of the DVR-based Wannier functions in Sec. V. In this section, we use these functions to study the two-body atom-atom interaction terms in the Hubbard model. So far, we have focused on the double-well lattice along the x axis. We can extend the calculations to the perpendicular directions and obtain the corresponding Wannier functions. Owing to the large band gap between the first and the second bands along perpendicular directions compared to that along the x direction, only the ground band is considered. Thus, the full three-dimensional-band Wannier functions are $w_\alpha(\vec{x}) = w_{j_c,\alpha}(x)w(y)w(z)$, where band index $\alpha \in \{1,2\}$ and $w(y)$ and $w(z)$ are the ground-band Wannier functions at the center of the lattice along the perpendicular directions. We note that the y and z Wannier functions have the same functional form as, for simplicity, we have

assumed the same lattice depth along the perpendicular directions. Similarly, the generalized Wannier functions are $v_\eta(\vec{x}) = v_{j_c,\eta}(x)w(y)w(z)$, where $\eta \in \{L,R\}$.

In the Hubbard model and band basis, the two-body on-site interaction energies are

$$U_{\alpha_1\alpha_2\alpha_3\alpha_4} = g\int w_{\alpha_1}(\vec{x})w_{\alpha_2}(\vec{x})w_{\alpha_3}(\vec{x})w_{\alpha_4}(\vec{x})d\vec{x}, \qquad (6)$$

where $g = 4\pi\hbar^2 a_s/m_a$, a_s is the s-wave scattering length and we use that the $w(\vec{x})$ are real. There are five distinct coefficients: U_{1111}, U_{1112}, U_{1122}, U_{1222}, and U_{2222}. On-site interaction energies $U_{\eta_1\eta_2\eta_3\eta_4}$ in the LR basis using the generalized Wannier functions $v_\eta(\vec{x})$ can be similarly defined. The five distinct interactions coefficients are U_{LLLL}, U_{LLLR}, U_{LLRR}, U_{LRRR}, and U_{RRRR}.

Figures 8(a) and 8(b) show the two-body interaction energies $U_{\alpha_1\alpha_2\alpha_3\alpha_4}$ and $U_{\eta_1\eta_2\eta_3\eta_4}$, respectively, for ^{87}Rb with $a_s = 5.3$ nm as a function of the lattice asymmetry b, with other lattice parameters kept fixed. Figure 8(a) is symmetric around $k_L b = \pi/4$. At the symmetry point $k_L b = \pi/4$, $U_{1111} \lesssim U_{1122} \lesssim U_{2222}$, while U_{1112} and U_{1222} are strictly 0 due to parity. As the lattice becomes asymmetric, U_{1111} and U_{2222} double their strength, U_{1122} rapidly decreases, and U_{1112} and U_{1222} have a maximum but remain relatively large.

Figure 8(b) shows that the $U_{\eta_1\eta_2\eta_3\eta_4}$ have a much smoother dependence on the asymmetry than the $U_{\alpha_1\alpha_2\alpha_3\alpha_4}$. For all asymmetries, we observe that U_{LLLL} and U_{RRRR} are much higher than the other energies. Moreover, $U_{LLLL} = U_{RRRR}$ for a symmetric lattice, and $U_{RRRR} > U_{LLLL}$ for $k_L b > \pi/4$. This behavior is reversed for $k_L b < \pi/4$. This is a consequence of the fact that $v_R(\vec{x})$ is more confined than $v_L(\vec{x})$ for $k_L b > \pi/4$, and vice versa. Interestingly, the density-induced tunneling energies U_{LRRR} and U_{LLLR} are, in general, higher than the density-density term U_{LLRR}. The former coefficients lead to terms in a Hubbard model where an atom hops from one well to the other in a unit cell, while the latter coefficient leads to either a long-range density-density interaction or pair hopping. The relative size of these energies highlights the limits of Hubbard models that do or do not include specific two-body terms [13].

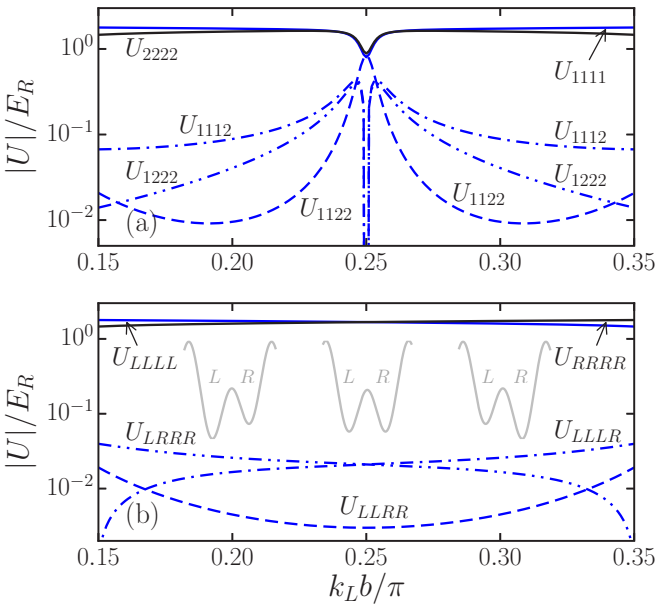

FIG. 8. Two-body interaction energies in the Hubbard model for ^{87}Rb in units of E_R as a function of the lattice asymmetry $k_L b/\pi$. We use $V_0/E_R = 35$, $V_1/V_0 = 1.3$, $V_2/E_R = 70$, and scattering length $a_s = 5.3$ nm. (a) Interaction energies $U_{\alpha_1\alpha_2\alpha_3\alpha_4}$ in the band basis with $\alpha \in \{1,2\}$. (b) Interaction energies $U_{\eta_1\eta_2\eta_3\eta_4}$ in the LR basis with $\eta \in \{L,R\}$. Insets: From left to right, schematic of a double-well potential for lattice asymmetries $k_L b < 0.25\pi$, $k_L b = 0.25\pi$, and $k_L b > 0.25\pi$, respectively.

The two-body interaction energies within the two bases can be compared in several limits of the lattice asymmetry. For $k_L b > \pi/4$ and very large asymmetries where $U_{1122} \ll U_{1111}$ the Wannier functions $w_1(\vec{x})$ approach $v_R(\vec{x})$ [similarly, $w_2(\vec{x})$ approaches $v_L(\vec{x})$], and thus, $U_{1111} \to U_{RRRR}$ and $U_{2222} \to U_{LLLL}$. In fact, for as low as $k_L b = 0.26\pi$, $U_{1111} \approx 0.95\, U_{RRRR}$. On the other hand, for a symmetric lattice we can write $w_{1,2}(\vec{x}) \approx (v_L(\vec{x}) \pm v_R(\vec{x}))/\sqrt{2}$ and $U_{LLLL} = U_{RRRR}$, which leads to $U_{1111}, U_{1122}, U_{2222} \approx U_{LLLL}/2$. The additional realization that U_{LLLL} and U_{RRRR} are nearly insensitive to asymmetry also explains the doubling in value of U_{1111} and U_{2222} near $k_L b = \pi/4$.

Even though the Wannier functions $w_1(\vec{x})$ and $v_R(\vec{x})$ approach each other for large asymmetries and $k_L b > \pi/4$, the function $v_R(x)$ is always more confined than $w_1(x)$. Consequently, the cross-terms U_{1122}, U_{1112}, and U_{1222}, which depend on the tail of the Wannier functions, are always larger than the corresponding cross-terms U_{LLRR}, U_{LLLR}, and U_{LRRR}.

VII. CONCLUSION

We have shown that real-valued Wannier functions can be efficiently constructed for both symmetric and asymmetric periodic potentials or optical lattices. The first step involves obtaining the single-particle band structure and real-valued eigenvectors using a discrete variable representation (DVR). A Fourier grid DVR based on basis functions with periodic boundary conditions is shown to have excellent numerical accuracy compared to a direct calculation based on plane waves. In the next step, restricted to eigenvectors within the subspace of band α, Wannier functions $w_\alpha(x)$ localized within a unit cell are obtained as eigenstates of the position operator. By using eigenvectors corresponding to the two lowest bands, generalized Wannier functions $w_\eta(x)$ localized to L and R wells within a double-well can also be constructed. By a comparison of the tunneling energies, the Wannier functions are shown to reproduce the Hubbard parameters with excellent accuracy. Tunneling energies are subsequently obtained between the L and the R wells using the generalized Wannier functions, and the limits of a tight binding containing only nearest-neighbor tunneling energies are discussed. Finally, we use these functions to study the two-body interaction energies in the BH model and discuss the relative importance of the various interaction energy terms. The numerical methods developed are general and can be applied to a wide array of optical lattice geometries in one, two, or three dimensions.

ACKNOWLEDGMENT

This work was supported by National Science Foundation Grant No. PHY-1506343.

[1] I. Bloch, J. Dalibard, and W. Zwerger, Rev. Mod. Phys. **80**, 885 (2008).
[2] D. Jaksch and P. Zoller, Ann. Phys. **315**, 52 (2005).
[3] D. Jaksch, C. Bruder, J. I. Cirac, C. W. Gardiner, and P. Zoller, Phys. Rev. Lett. **81**, 3108 (1998).
[4] M. Greiner, O. Mandel, T. Esslinger, T. W. Hänsch, and I. Bloch, Nature **415**, 39 (2002).
[5] J. Sebby-Strabley, M. Anderlini, P. S. Jessen, and J. V. Porto, Phys. Rev. A **73**, 033605 (2006).
[6] P. J. Lee, M. Anderlini, B. L. Brown, J. Sebby-Strabley, W. D. Phillips, and J. V. Porto, Phys. Rev. Lett. **99**, 020402 (2007).
[7] S. Trotzky, P. Cheinet, S. Fölling, M. Feld, U. Schnorrberger, A. M. Rey, A. Polkovnikov, E. A. Demler, M. D. Lukin, and I. Bloch, Science **319**, 295 (2008).
[8] M. Atala, M. Aidelsburger, J. T. Barreiro, D. Abanin, T. Kitagawa, E. Demler, and I. Bloch, Nat. Phys. **9**, 795 (2013).
[9] L. Tarruell, D. Greif, T. Uehlinger, G. Jotzu, and T. Esslinger, Nature **483**, 302 (2012).
[10] G.-B. Jo, J. Guzman, C. K. Thomas, P. Hosur, A. Vishwanath, and D. M. Stamper-Kurn, Phys. Rev. Lett. **108**, 045305 (2012).
[11] K. L. Lee, B. Grémaud, R. Han, B.-G. Englert, and C. Miniatura, Phys. Rev. A **80**, 043411 (2009).
[12] T. Uehlinger, G. Jotzu, M. Messer, D. Greif, W. Hofstetter, U. Bissbort, and T. Esslinger, Phys. Rev. Lett. **111**, 185307 (2013).
[13] O. Jürgensen, K. Sengstock, and D.-S. Lühmann, Phys. Rev. A **86**, 043623 (2012).
[14] D.-S. Lühmann, O. Jürgensen, and K. Sengstock, New J. Phys. **14**, 033021 (2012).
[15] U. Bissbort, F. Deuretzbacher, and W. Hofstetter, Phys. Rev. A **86**, 023617 (2012).
[16] S. Paul and E. Tiesinga, Phys. Rev. A **92**, 023602 (2015).
[17] W. Kohn, Phys. Rev. **115**, 809 (1959).
[18] G. H. Wannier, Rev. Mod. Phys. **34**, 645 (1962).
[19] S. Paul and E. Tiesinga, Phys. Rev. A **88**, 033615 (2013).
[20] N. Marzari and D. Vanderbilt, Phys. Rev. B **56**, 12847 (1997).
[21] N. Marzari, A. A. Mostofi, J. R. Yates, I. Souza, and D. Vanderbilt, Rev. Mod. Phys. **84**, 1419 (2012).
[22] B. Vaucher, S. R. Clark, U. Dorner, and D. Jaksch, New J. Phys. **9**, 221 (2007).
[23] M. Modugno and G. Pettini, New J. Phys. **14**, 055004 (2012).
[24] J. Ibañez-Azpiroz, A. Eiguren, A. Bergara, G. Pettini, and M. Modugno, Phys. Rev. A **88**, 033631 (2013).
[25] R. Walters, G. Cotugno, T. H. Johnson, S. R. Clark, and D. Jaksch, Phys. Rev. A **87**, 043613 (2013).
[26] J. Ibañez-Azpiroz, A. Eiguren, A. Bergara, G. Pettini, and M. Modugno, Phys. Rev. A **87**, 011602 (2013).
[27] D.-S. Lühmann, O. Jürgensen, M. Weinberg, J. Simonet, P. Soltan-Panahi, and K. Sengstock, Phys. Rev. A **90**, 013614 (2014).
[28] S. Kivelson, Phys. Rev. B **26**, 4269 (1982).
[29] D. T. Colbert and W. H. Miller, J. Chem. Phys. **96**, 1982 (1992).
[30] V. Szalay, J. Chem. Phys. **99**, 1978 (1993).
[31] E. Tiesinga, C. J. Williams, and P. S. Julienne, Phys. Rev. A **57**, 4257 (1998).
[32] R. G. Littlejohn, M. Cargo, T. Carrington, Jr., K. A. Mitchell, and B. Poirier, J. Chem. Phys. **116**, 8691 (2002).
[33] V. Szalay, G. Czakó, A. Nagy, T. Furtenbacher, and A. G. Császár, J. Chem. Phys. **119**, 10512 (2003).
[34] N. Nygaard, G. M. Bruun, B. I. Schneider, C. W. Clark, and D. L. Feder, Phys. Rev. A **69**, 053622 (2004).
[35] M. L. Wall, K. R. A. Hazzard, and A. M. Rey, Phys. Rev. A **92**, 013610 (2015).